Paleobiology, 33(3), 2007, pp. 382–396

Growth modes of 2-Ga microfossils

Steven Bennett, David Boal, and Hanna Ruotsalainen

Abstract.—By digitally imaging colonies with more than a hundred cells, the distributions of cell size and shape are determined for four examples of 2-Ga microfossils: bacillus-shaped *Eosynechococcus moorei* and three dyads or diplococci (*Sphaerophycus parvum* and two forms of *Eoentophysalis belcherensis*). By assuming that each colony obeys steady-state growth, the measured distributions can be inverted to infer the time evolution of the individual cell shape. The time evolution can also be predicted analytically from rate-based models of cell growth, permitting the data to distinguish among different postulates for the physical principles governing growth. The cell cycles are found to be best described by the exponential growth of cell volume, although linear volume growth is not ruled out. However, the measured dyad cycles are inconsistent with several growth models based on surface area or the behavior of the septum at the division plane. Where they have been measured, modern bacilli obey exponential growth whereas eukaryotics obey linear growth, which implies that these 2-Ga microfossils are likely prokaryotic.

Steven Bennett, David Boal, and Hanna Ruotsalainen. Department of Physics, Simon Fraser University, Burnaby, British Columbia V5A 1S6, Canada. E-mail: boal@sfu.ca*
**Corresponding author*

Accepted: 6 April 2007

Introduction

The record of the emergence of life on Earth includes isotopic ratios typical of biological processes (Schidlowski 1988; Mojzsis et al. 1996; Rosing 1999; Shen et al. 2001; for a recent critique, see van Zuilen et al. 2002) and fossilized cell colonies and other remnants, of which some have been dated at 3.5–3.0 Ga (Knoll and Barghoorn 1977; Walsh and Lowe 1985; Schopf and Packer 1987; Schopf 1993; Rasmussen 2000; Furnes et al. 2004) and others at 2.5–2.0 Ga (Barghoorn and Tyler 1965; Hofmann 1976; Knoll and Barghoorn 1976; Timofeev 1979). Individual microfossils display shapes such as ellipsoids, dyads (diplococci, or pairs of joined spheres), rodlike bacilli, and filamentous tubes and rods; collectively, they may be found in loose colonies or dense mats. Lost during the fossilization process, their internal architecture is largely unknown compared to the design and construction of modern cells (Boal 2002). What, then, can be learned about their mechanical features or cell cycle when so few of the techniques for probing modern cells are applicable?

Many taxa of microfossils have been imaged photographically to permit the determination of ensemble-averaged quantities such as the mean cell width or eccentricity. Valuable as these averaged quantities are for characterization purposes, the underlying probability distributions of cell sizes and shapes are substantially more informative because they may be used to infer the cell cycle of the measured population as described below. At least three conditions need to be satisfied for such an analysis to succeed:

1. the shapes must be accurately determined;
2. for conventional microscopy, the random orientation of cells must be taken into account;
3. the cell colonies must be sufficiently large as to obey steady-state growth, such that the observed cells provide a statistically appropriate sample of the cell cycle.

Digital imaging with a CCD camera lends itself to the application of numerical algorithms that resolve item (1), as will be described below. The formalism needed to accommodate item (2) is straightforward and described in the Appendix. As for item (3), there are several examples of microfossils in the 2–2.5 Ga age range where colonies of cells have not been subject to large-scale shear stress and can be imaged without excessive background. In summary, items 1–3 can be addressed, permitting the study of microfossil shape to help

 0094-8373/07/3303-0002/$1.00

identify relationships between the architecture and cell cycle of microfossil taxa and their modern analogues.

A theoretical framework is needed to interpret the inferred cell cycle and expose the physical and biological principles that drive it. One starting point for the mathematical description of a cell cycle would be a set of rate equations governing the production of molecular building blocks such as lipids and proteins, and their incorporation into the cell's mechanical components such as the plasma membrane or cell wall. In this paper, we describe these manufacturing and assembly processes through a set of empirical rate equations (for example, various postulates for the growth rates of the cell area or volume), although we cannot directly establish the actual magnitudes of the rate constants appearing in the differential equations. Each rate equation (such as $dA/dt \propto A^n$, where A is the surface area of the cell and n is a tunable exponent) leads to a prediction for the time-dependence of a geometrical attribute such as the cell size or shape. In other words, although this theoretical approach cannot predict the absolute time scale for the cell cycle, it can predict the probability distributions for measurable attributes, allowing experiment to select among various models and principles for cell growth.

Not all geometrical quantities are useful descriptors of the cell cycle. Much of what is known of the cycle of modern bacteria comes from studies of uniform cylindrical cells, whose shapes provide only limited information about the cell cycle because their length, surface area and volume are all roughly linearly proportional. That is, a cylindrical shape cannot discriminate easily among models in which the cell cycle is driven by one of cell length, area, or volume, because all three quantities have similar time dependence. However, this is not true of dyads, whose volume is not linearly proportional to cell area or length. Fortunately, both dyadic and rodlike cell shapes are common among microfossils, providing a good laboratory for investigating the evolution of the cell cycle over several billion years. What is known so far from modern cells is that cylindrical bacteria are observed to extend *exponentially* with time along their symmetry axis (reviewed in Bramhill 1997); examples include *Bacillus cereus* (Collins and Richmond 1962), *Escherichia coli* (Koppes and Nanninga 1980), and *Bacillus subtilis* (Sharpe et al. 1998). In contrast, the mass of modern eukaryotic cells increases *linearly* with time (Killander and Zetterberg 1965). The reader is referred to Murray and Hunt (1993) or Hall et al. (2004) for broader treatments of the cell growth process.

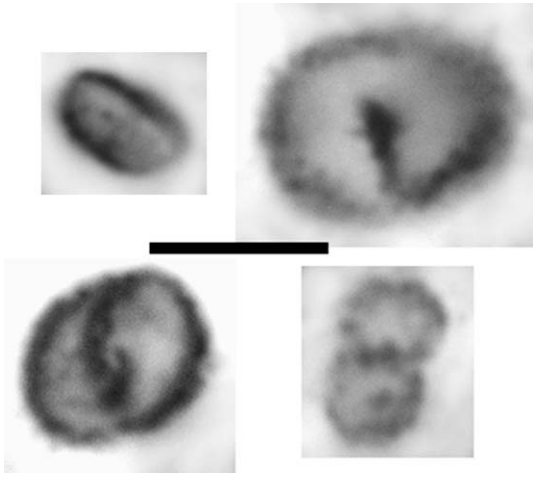

FIGURE 1. Examples of Belcher Island microfossils. Clockwise from the upper left: bacillus-like *E. moorei* and dyads *EB*, *S. parvum*, and *E. belcherensis capsulata*. Scale bar, 5 microns.

In this paper, we measure the shapes of four examples of 2-Ga microfossils collected from Canada's Belcher Islands (Hofmann 1976): bacillus-like *Eosynechococcus moorei* Hofmann, 1976, and three dyads, *Sphaerophycus parvum* Schopf 1968, *Eoentophysalis belcherensis capsulata* Hofmann, 1976, and a cell type that we label *EB* (not cataloged in the collection but resembling *Eoentophysalis belcherensis punctata* Hofmann, 1976, which is a degradational variant of *Eoentophysalis belcherensis*). The cell shapes in this collection appear to have suffered little deformation by geological events following fossilization; although the cells may have suffered plasmolysis and degradation, we assume that this has affected all cells in a similar way. Figure 1 shows examples of each cell colony, where the individual cell dimensions are most commonly in the 2–9 μ range. These cells grow primarily along their symmetry axis, which appears to be randomly ori-

ented in the colonies studied. In some cases, the cell interiors contain dark regions which might be adventurously interpreted as remnants of nuclei but are almost certainly degradational features (Golubic and Hofmann 1976); with an age of about 2 Ga, these cells originate from the epoch when eukaryotes were thought to increase in abundance along with the rise in atmospheric oxygen. We will show that the cell cycle inferred from the distribution of cell shapes most closely resembles the growth of modern prokaryotes.

Containing results from several experimental, analytical, and numerical techniques, this paper is organized as follows:

1. Following an introduction to the source of the microfossil colonies, the image analysis algorithm is described at length because of its importance for obtaining accurate shape distributions.
2. With this imaging technique, the cell shape characteristics are reported for the four cell types of interest; all taxa exhibit relatively constant surface curvature during cell growth.
3. Five different growth-rate models for the cell cycle are introduced and solved analytically. The method for angle-averaging the cell orientations to permit comparison with experiment is straightforward, although it must be done numerically in some situations. We argue that dyadic taxa are best suited for distinguishing among various models for cell growth.
4. We show that the cycles of individual cells in all taxa are consistent with exponential volume growth, meaning that the rate at which the cell volume increases is proportional to the cell's volume (that is, $dV/dt \propto V$). Most other growth models are clearly inconsistent with the observed distributions of cell shape, although linear volume growth is not ruled out.
5. Last, we illustrate how the data can be probed further by means of a computer simulation of the cell cycle that could incorporate a two-step growth process for dyads as well as some aspects of experimental uncertainties, etc. As it stands, more accurate data are needed to make quantitative use of the simulation approach.

Although the focus of this paper is the elucidation of the microfossil cell cycle, nevertheless the techniques described are generic and applicable to any population of cells obeying steady-state growth.

Material

The microfossils analyzed here are from cherts collected in the Belcher Islands of Hudson Bay by Hans Hofmann (1976) and are curated at the Geological Survey of Canada (GSC). First proposed to contain the fossilized remains of ancient cells by Moore (1918), the formations are roughly two billion years old: the overlying strata are 1.760 ± 0.037 Ga (Fryer 1972; recalculated) and the underlying basement is older than 2.5 Ga. The samples are drawn mainly from the McLeary and Kasegalik Formations at several different stratigraphic levels, as described in more detail by Hofmann (1976). Found in black chert in stromatolitic dolostones, the sedimentary structures indicate deposition in supratidal, intertidal and subtidal environments undergoing gradual subsidence. Modern analogues are intertidal and subtidal algal mats and mounds (Golubic and Hofmann 1976). Hofmann (1975) argues that these stromatolites are formed by permineralization of algal mats by amorphous or gelatinous silica and carbonate, followed by crystallization and recrystallization. In the 18 thin sections of the collection, Hofmann (1976) has identified and cataloged examples of 24 cell taxa, some of which may be degradational products of others.

For the purposes of this analysis, we have scanned the collection manually for loosely associated colonies of undistorted cells; large growth fronts of more than 10^4 cells were not included in our analysis, in part because the cells are distorted by contact with their neighbors. The coordinates of each colony presented here, and the number n of cells or cell pairs imaged from it, are as follows: *Eosynechococcus moorei* ($n = 224$; GSC42770 at $26.6x$, $14.5y$); *Sphaerophycus parvum* ($n = 99$; GSC42773 at $17.9x$, $10.0y$); *Eoentophysalis belcherensis capsulata* ($n = 156$; GSC42773 at $17.1x$, $8.3y$); and an

uncataloged colony which we will refer to as *EB*, similar to *Eoentophysalis belcherensis punctata* ($n = 184$; GSC42769 at 38.4x, 20.6y). The five-digit number is the GSC identification of the microscope slide, and the xy coordinates are displacements in millimeters from its upper right-hand corner. To gauge the variation of cell shape with local environment, we imaged additional colonies of *E. moorei* from different locations: ($n = 271$; GSC42769 at 32.4x, 7.3y) and ($n = 76$; GSC43589 at 26.2x, 9.9y). Where the cells in a colony display an axis of cylindrical symmetry, their orientation appears to be random; that is, they are not arranged radially with respect to the center of the cell colony. The taxa examined appear commonly in the Belcher Island samples (Hofmann 1976) and should not be regarded as unusual or exotic; our particular choice of colony was motivated only by numerical size and clarity of images.

Methods

Our determination of cell shape distributions requires an image analysis method that yields accurate and numerically stable measurements of cell dimensions. Each cell colony is examined microscopically (Olympus BX51) with oil immersion objectives of 50× or 100× magnification at 1 μm steps in the z-direction, perpendicular to the focal plane. As the colonies may be hundreds of microns across, they are subdivided into 50–100 μm regions for image capture with a CoolSnap *cf* © CCD camera (Roper Scientific) having pixels of 4.65 μm to the side. From these regional domains, individual cell images are extracted, having dimensions of 60–250 pixels in a given direction. To reduce their interference with algorithms for determining the cell boundary, segments of nearby cells appearing in an image are removed manually using Adobe Photoshop© image manipulation software. Obviously incomplete cells and those near the boundary of the thin section are discarded to reduce sample bias (Smith 1968 outlines the problem of determining the mean dimensions of 200–400 μm diameter grains embedded in thin sections). Grayscale values of the Cartesian CCD image are then translated, by using a Monte Carlo sampling approach, into a polar coordinate representation with origin at the cell's visual center of mass. Commonly, a cell appears as a dark ring with a light interior, or a dark disk on a light background; in either case, the somewhat diffuse outer boundary is about 5–8 pixels thick, across which the grayscale value decreases away from the cell center (here, black and white have grayscale values of 255 and 0, respectively).

A numerical algorithm provides a systematic quantification of cell shape and reduces the likelihood of subjective biases from the observer. Working in the polar coordinate representation, the numerical derivative $d_{i\alpha}$ of a series of grayscale density values $g_{i\alpha}$ is determined simply from $d_{i\alpha} = (g_{i+1,\alpha} - g_{i-1,\alpha})/2$, where i is a radial pixel index at fixed polar angle α (measured with respect to the vertical axis of the image). Searching from the coordinate origin, the location of the radial pixel m with the most negative derivative $d_{m\alpha}$ is determined for each α, corresponding to the outer edge of the cell. From m, the radial location of the boundary r_α at angle α is constructed from a weighted average of derivative pixels around m, namely $r_\alpha = \Sigma_j\, r_j d_{j\alpha}/\Sigma_j\, d_{j\alpha}$, where the radial index j satisfies $m - 2 \le j \le m + 2$ and only negative values of $d_{j\alpha}$ are included in the sum. Consistent with the dimensions of the boundary mentioned above, these five pixels cover most of the diffuse outer edge of the cell image. Lastly, the suite of values $\{r_\alpha\}$ for each cell image is fitted by a Legendre polynomial expansion $R(\gamma) = \Sigma_l\, c_l P_l\,(\cos\gamma)$, where the polynomial index satisfies $0 \le l \le 4$ and where c_l are coefficients with the dimension of length. The angle γ is defined with respect to one of the cell's symmetry axes (almost always prolate) obtained by diagonalizing the ''inertia tensor'' of the cell boundary generated from $\{r_\alpha\}$. That is, the representation $R(\gamma)$ is a continuous function of angle γ, which permits the cell's shape to be determined more accurately than the discrete set of points $\{r_\alpha\}$.

The main sources of error in the algorithm include (1) small irregularities in the cell boundary on the submicron length scale arising from the fossilization process, and (2) slight smearing of the boundary by the CCD discretization and conversion to the polar representation. The extracted boundary typically

drifts by ±1% when the size of the polar bins is varied, although changes up to ±2% are occasionally observed. A change in the coordinate bin size tends to shift the sizes of all cells in a colony by a similar scale factor, so that the relative distribution of sizes is less sensitive to this uncertainty. We find for these images that 32 angular bins and 40 to 50 radial bins produce robust fits.

Results and Discussion

Our approach to the study of microfossil cell cycles involves three different toolkits, so to speak—image analysis, analytical modeling, and computer simulation—all reported in this one section of the paper. To clarify the presentation, our results are organized into the following subsections:

a. distributions of cell sizes and shapes as obtained from microfossil images,
b. analytical predictions for these distributions from rate-based models for cell growth,
c. determination of cell cycles consistent with the measured cell colonies, and
d. simulation of correlations in cell shape which could probe multistep cell cycles.

Of these, subsections (b) and (d) are of general applicability to equilibrium populations of cells.

Size and Shape Distributions.—As observed microscopically for the colonies analyzed, the three-dimensional shape of each cell or cell pair appears to have an axis of rotational symmetry. Figure 2 shows two views of the same dyad: the ''top view'' is its appearance as a pair of overlapping spheres (as seen through a microscope), whereas the ''side view'' is drawn perpendicular both to the symmetry axis of the dyad and to the viewing direction (that is, within the plane of a thin section). The symmetry axis makes an angle θ with respect to the viewing axis. Now, the symmetry axis seems to be randomly oriented in the samples studied, such that an average must be performed over θ when comparing measurements with analytical models; this will be treated in the following subsection. Generally speaking, it is easier to predict analytically the properties of projected shapes of the whole

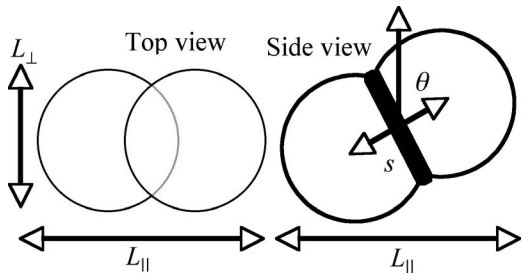

FIGURE 2. Definition of projected lengths $L_\perp$ and $L_\parallel$ used in the shape analysis of a dyad. The top view is the appearance of an overlapping cell pair in a dyad as seen through a microscope. The side view is the same pair as seen in the plane of the thin section, perpendicular to the cylindrical symmetry axis of the dyad. The separation between centers of the spherical caps is s, while θ is the angle between the symmetry axis and the direction of observation. The side view shows that the projected length $L_\parallel$ is equal to $2R + s \sin\theta$; the projected width is $L_\perp = 2R$, independent of θ. The thick line indicates the junction of the two caps; referred to as the neck, this junction region is circular with a radius r.

cell rather than slices through it, particularly when angle-averaging must be performed. As a result, we focus on the projected lengths $L_\perp$ and $L_\parallel$, perpendicular and parallel to the cell's projected symmetry axis as defined in Figure 2. For a dyad pair, where each subunit has radius R and their centers of curvature are separated by a distance s, one can see that $L_\perp = 2R$ independent of s or θ, and $L_\parallel = 2R + s\cdot\sin\theta$.

Turning first to the dyadic taxa, a large fraction of cells in these colonies have the appearance of two spherical caps joined at a ring; the percentage of visible dyads is roughly 45% or more for all dyadic taxa reported in Table 1. Dyads with their symmetry axis lying close to the direction of observation will not appear as linked cells, but rather as one mildly elliptical object with a thick boundary, so the measured fraction underestimates the true fraction by a small percentage. That these cells spend 50% or more of their life as dyads indicates that they are *not* described by a cell cycle in which the cell slowly inflates radially like a balloon before it rapidly contracts along an equatorial arc to form two daughters; cells in such a cycle would be dyads for only a small fraction of time.

We now examine the projected shapes of all four cell types of interest. The images are obtained by using a microscope objective with a

TABLE 1. Percentage of visible dyads and lengths $L_\perp$ and $L_\parallel$ of projected cell shapes for four microfossils colonies with n analyzable cells or pairs. Data are quoted as ⟨mean⟩ ± (σ = standard deviation). The mean values are obtained from specific colonies, and may vary from one colony to the next depending on growth conditions.

Visible dyads	$\langle L_\perp \rangle$ (μm)	$\sigma_\perp/\langle L_\perp \rangle$	$\langle L_\parallel \rangle$ (μm)	$\sigma_\parallel/\langle L_\parallel \rangle$	$\langle L_\parallel/L_\perp \rangle$
Sphaerophycus parvum (dyads, n = 99)					
45 ± 7%	2.82 ± 0.28	0.10	3.62 ± 0.60	0.17	1.28 ± 0.18
Eoentophysalis belcherensis capsulata (dyads, n = 156)					
72 ± 7%	4.96 ± 0.59	0.12	6.68 ± 1.16	0.17	1.35 ± 0.18
EB (dyads, n = 184)					
43 ± 5%	5.90 ± 0.54	0.092	7.63 ± 1.24	0.16	1.30 ± 0.19
Eosynechococcus moorei (rods, n = 224)					
no meaning	2.71 ± 0.31	0.12	3.85 ± 0.67	0.17	1.43 ± 0.24

large enough depth of field to capture the shape as projected onto the viewing plane (100× for the small *E. moorei* and *S. parvum* and 50× for the larger cells). The observations are summarized in Table 1, where σ is the standard deviation of a distribution, and n is the number of objects in the analysis. The mean projected width $\langle L_\perp \rangle$ varies considerably, ranging from just under 3 μm for *E. moorei* and *S. parvum* to 5 μm for *E. belcherensis capsulata* and 6 μm for *EB*. Even though the colonies represent cells of moderately different mean sizes, the ratio of the standard deviation of the distribution of $L_\perp$ to its mean $\langle L_\perp \rangle$ is quite constant: $\sigma_\perp/\langle L_\perp \rangle$ = 0.12, 0.10, 0.12, and 0.092 for the four colonies, in order of increasing $\langle L_\perp \rangle$. However, the observed distribution is broadened by the fuzzy biological boundary of the original living cell, the effects of degradation during fossilization, and the uncertainties of the measurement process, so these ratios are an *overestimate* of the native ratios before cell death. Lastly, we note that the mean values of these geometric quantities may drift by perhaps 10% from one colony of cells to the next for the same taxon, judging from the behavior we observed for three different colonies of *E. moorei*. Such differences are presumably attributable to variation of the local environments in which the cells grew.

To probe the distributions of $L_\perp$ further, we repeat the shape analysis on the individual subunits of dyads using the same colonies as Table 1. Now, the subunits are captured by using an objective (100×) having a narrow depth of field; following image capture, the boundaries of any connected subunits are removed from the image manually. Comparing the results with Table 1, we find $\langle L_\perp \rangle \pm \sigma_\perp$ of the subunits is: 2.80 ± 0.28 μm for *S. parvum* (n = 78), 4.57 ± 0.51 μm for *E. belcherensis capsulata* (n = 279) and 5.89 ± 0.47 μm for *EB* (n = 155), where $L_\perp$ and $\sigma_\perp$ have the same meaning as Table 1 but n includes individual subunits as well as complete cells for those situations where resolution into subunits is impossible. We first observe that $\langle L_\perp \rangle$ and $\sigma_\perp$ are fairly similar for both the separated subunits and the complete dyads of Table 1. This gives us confidence that our imaging techniques and analysis are robust, as the two data sets for each colony were imaged, extracted, and numerically analyzed independently. Important for their interpretation, the distributions in $L_\perp$ are even narrower than those of the intact cells of Table 1: for the subunits, $\sigma_\perp/\langle L_\perp \rangle$ = 0.10, 0.11, and 0.080. As for Table 1, these numbers overestimate the native ratios before cell death.

A more informative probe of cell width is the probability density $\mathcal{P}_\perp$ for the projected width $L_\perp$, where $\mathcal{P}_\perp$ has units of inverse length and is normalized to unity via $\int \mathcal{P}_\perp \, dL_\perp = 1$. Figure 3 compares $\mathcal{P}_\perp$ of small *E. moorei* (solid line) and larger *EB* (dashed line). Clearly, $\mathcal{P}_\perp$ does not correspond to a uniform distribution in $L_\perp$, even allowing for some smearing arising from fossilization and measurement effects. Rather, $\mathcal{P}_\perp$ resembles a sharply peaked native distribution, which has been broadened by a Gaussian function with $\sigma \sim 0.1$. Thus, the ratio $\sigma_\perp/\langle L_\perp \rangle$ of the subunits and the distribution $\mathcal{P}_\perp$ of all taxa both point toward a rather narrow distribution in cell width during the

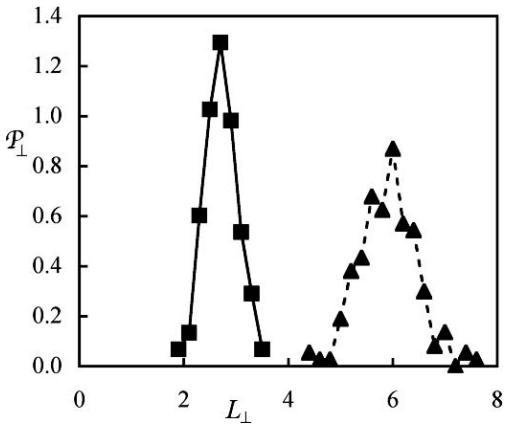

FIGURE 3. Measured probability density $\mathcal{P}_\perp$ of the transverse dimension $L_\perp$ for small bacillus-shaped *E. moorei* (solid line, $n = 224$) and large dyads *EB* (dashed line, $n = 184$). The peaks have about 30 cells per bin, resulting in a statistical uncertainty of about 20% for $\mathcal{P}_\perp$ at its peak. Dimensions are microns for $L_\perp$ and inverse microns for $\mathcal{P}_\perp$.

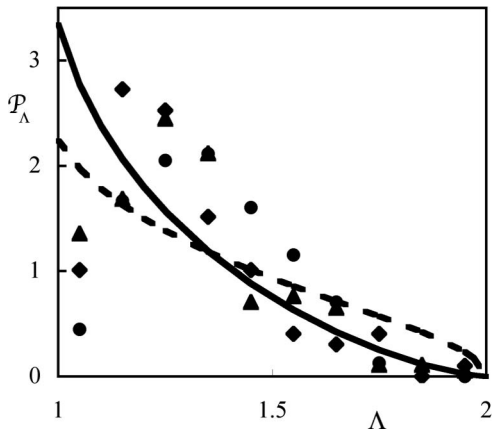

FIGURE 4. Combined data for the probability density $\mathcal{P}_\Lambda$ of the dyads *S. parvum* (diamonds), *E. belcherensis capsulata* (circles), and *EB* (triangles) compared with the expectations of growth at constant curvature and exponential increase in volume (solid curve) or area (dashed curve). The largest values of $\mathcal{P}_\Lambda$ have about 30 cells per data bin for a statistical uncertainty of about 20% per individual datum.

cell cycle for dyads and for rodlike *E. moorei*. This is consistent with $\sigma_\perp/\langle L_\perp\rangle \sim 0.10$ in modern *B. subtilis*, which grows by elongation, not radial inflation (Sharpe et al. 1998). Measurements of seven taxa of modern diplococcal and rodlike cyanobacteria yield $\sigma_\perp/\langle L_\perp\rangle = 0.07$ to 0.10 (C. Forde and D. H. Boal unpublished data).

Cells of the microfossil taxa studied here are not generally spherical in shape, and this is reflected in the values of the mean projected length $\langle L_\parallel\rangle$ compared to $\langle L_\perp\rangle$. As reported in Table 1, $\langle L_\parallel\rangle$ is 30–40% higher than $\langle L_\perp\rangle$ for the dyads and *E. moorei*. A slightly more sensitive ratio than $\langle L_\parallel\rangle/\langle L_\perp\rangle$ is the ensemble average $\langle L_\parallel/L_\perp\rangle$ which has the experimental advantage of lower systematic uncertainties through the use of the dimensionless ratio $\Lambda = L_\parallel/L_\perp$ on a cell-by-cell basis. As seen in Table 1, $\langle\Lambda\rangle$ is approximately 1.3 for dyads and somewhat more than 1.4 for rodlike cells; $\langle\Lambda\rangle$ is expected to be larger for rodlike cells because the cylindrical section of the cell has a non-zero minimum value (whereas dyads are pairs of truncated spheres). Measurements of several modern cyanobacteria yield $\langle\Lambda\rangle = 1.3$ to 1.5 for diplococci and 1.8 to 2.4 for long rodlike cells (C. Forde and D. H. Boal unpublished data). Given that the averaging process includes orientations with small values of θ, the mean projected length $\langle L_\parallel\rangle$ is obviously less than the actual mean length, and this is particularly true for rodlike cells. For both dyads and bacilli, the upper bound on $L_\parallel/L_\perp$ is at least 2, so there should be a broader distribution in $L_\parallel$ than in $L_\perp$. This behavior can be seen in Table 1, where the relative width $\sigma_\parallel/\langle L_\parallel\rangle$ is about 0.17 for all examples, compared with $\sigma_\perp/\langle L_\perp\rangle$ of about 0.11.

Rather than probing the shapes further using the probability density $\mathcal{P}_\parallel$ (with units of inverse length), we work with the unitless probability density $\mathcal{P}_\Lambda$ generated from $\Lambda = L_\parallel/L_\perp$. In Figure 4, $\mathcal{P}_\Lambda$ for the three colonies of dyads is seen to rise rapidly to a maximum exceeding $\mathcal{P}_\Lambda = 2.5$ at Λ near 1 before falling more gently as Λ approaches its upper limit of 2 for linked spheres. In contrast, $\mathcal{P}_\Lambda$ for the bacillus-like *E. moorei* in Figure 5 does not exhibit such a pronounced peak, rising only to $\mathcal{P}_\Lambda = 1.5$; further, $\mathcal{P}_\Lambda$ for this rodlike shape persists above the dyad data at larger Λ and continues beyond $\Lambda = 2$ as permitted by geometry. In both figures, $\mathcal{P}_\Lambda$ is normalized to unity by $\int \mathcal{P}_\Lambda\, d\Lambda = 1$. Comparing Figure 3 with either of Figures 4 and 5 demonstrates the breadth of the distribution in $L_\parallel$, and confirms the observation that values for $\sigma_\parallel/\langle L_\parallel\rangle$ are larger than those of $\sigma_\perp/\langle L_\perp\rangle$ obtained from the much narrower distribution $\mathcal{P}_\perp$. We now use $\mathcal{P}_\Lambda$ to discriminate among models for cell growth; we

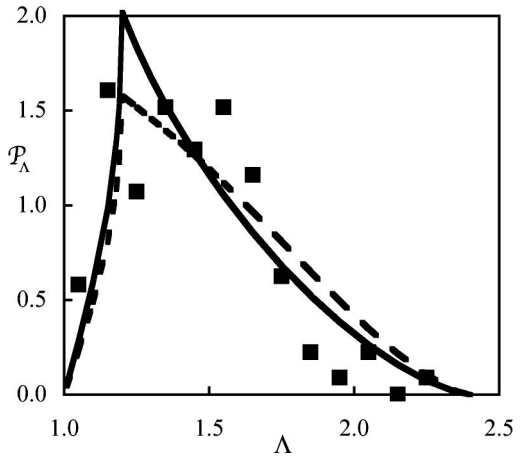

FIGURE 5. Measured probability density $\mathcal{P}_\Lambda$ for the bacillus-like *E. moorei* compared with predictions from exponential (solid curve) and linear (dashed curve) volume growth for spherocylinders ($\beta_0 = 0.2$). Statistical uncertainties as in Figure 4.

return to correlations in $L_\parallel$ and $L_\perp$ in a later subsection.

Models for the Cell Cycle.—In an ideal world, the measured probability densities $\mathcal{P}$ from image analysis would be sufficiently accurate that they could be numerically integrated to obtain the time evolution of the cell shape—the geometrical description of the cell cycle. Two aspects of the measurement serve to confound this approach:

1. the distributions are limited in their accuracy, in part because the colonies suitable for imagery contain only a few hundred cells; and
2. by measuring projected shapes, one is forced to include orientational averaging.

The method of choice, then, is to work from the opposite direction by proposing analytical models for the cell cycle from which the functions $\mathcal{P}$ can be predicted, including orientational averaging.

To model the cell cycle, we hypothesize a rate equation for a geometrical quantity (for example, $dV/dt \propto V$, where V is the cell volume) and solve it to determine the time evolution of the quantity. For an arbitrary cell shape, the length, surface area, and enclosed volume each can obey a different rate equation and hence display different time dependence during cell growth. However, by imposing constraints on the general cell shape, these quantities become related so that the time evolution of the cell shape depends on the behavior of only one or two independent geometrical characteristics. Specifically, we interpret $\sigma_\perp/\langle L_\perp \rangle \sim 0.10$ of dyad subunits to mean that the curvature of the cell boundary is fairly constant during cell growth; this constraint is sufficient to reduce the number of independent variables to just one for both dyads and spherocylinders. That is, once the time evolution of just one of separation $s(t)$, area $A(t)$, or volume $V(t)$ is known, where s is defined on Figure 2, the remainder are determined by the constraint of growth at constant curvature.

Mathematically, our approach is to

1. propose a simple rate equation for one of s, A, V or some other shape characteristic;
2. solve for the time-dependence of that characteristic using the rate equation from (1);
3. determine $s(t)$ using the solution in (2) under the assumption that surface curvature is constant during growth.

Knowing $s(t)$ from (3), the probability density $\mathcal{P}_s$ in s under steady-state conditions can be calculated from

$$\mathcal{P}_s = (dt/ds)/T_2, \tag{1}$$

where T_2 is the doubling time of the cycle. As an example, the simplest case for dyads is linear growth in s, or $s(t) = 2Rt/T_2$; this gives $ds/dt = 2R/T_2$ and hence $\mathcal{P}_s = (2R)^{-1}$ from equation (1). The assumption of steady-state growth is central to the analysis, as it relates the probability density to the time evolution of the cell shape. Most readers encountered a form of equation (1) when introduced to simple harmonic motion, where the probability of observing an object at a given displacement during an oscillation is inversely proportional to its speed at that point: an object is more likely to be observed at a turning point where its speed is low than at zero displacement where its speed is high. Equation (1) can be integrated to confirm the normalization of $\mathcal{P}_s$.

For dyads, s and A are linearly proportional to each other (and thus are not independent), but not to the volume nor to the radius r of the circular neck at the division plane. Hence, it is redundant to consider separate models for s

and A; rather, we propose several growth models each of which treats as an independent variable just one of cell area, cell volume, or radius r of the septum defining the division plane. This approach assumes that division is symmetric and occurs at a unique time T_2; as discussed below, our data are not sufficiently accurate to isolate and identify the effects of distributions in division time or daughter size, as considered by Koch and Schaechter (1962), Rosenberger et al. (1978) or Sharpe et al. (1998), for example. With their limited ability to distinguish among rate models for s, A, or V, only two growth models are considered for bacillus-like shapes: either linear or exponential increase in the volume with time.

Care must be taken to average over the angle θ of the cell symmetry axis with respect to the direction of observation, a process that reduces the mean projected length. As a simple example, consider a set of identical thin rods of length L_R and negligible radius. The mean projected length of a randomly oriented collection of such rods is $\langle L_\parallel \rangle = \{\int_0^1 L_R \sin\theta\, d\cos\theta\}/\{\int_0^1 d\cos\theta\} = (\pi/4)L_R$; that is, $\langle L_\parallel \rangle$ is about 20% smaller than L_R. Although important, this reduction is modest because, in a random distribution, there are far fewer ''vertical'' orientations (toward the viewer) than orientations close to the focal plane. As established in the Appendix, the angle-averaged probability density $\mathcal{P}_\Lambda$ for the dimensionless projected length Λ can be obtained from

$$\mathcal{P}_\Lambda = \int \mathcal{P}_\beta \frac{[(\Lambda - 1)/\beta]}{[\beta^2 - (\Lambda - 1)^2]^{1/2}}\, d\beta, \qquad (2)$$

where the dimensionless integration variable β is defined by $\beta = s/2R$ such that $\mathcal{P}_\beta = 2R\mathcal{P}_s$. The integration limits are provided in the Appendix. In other words, once $\mathcal{P}_s$ has been obtained for a given model, it leads to a prediction for $\mathcal{P}_\Lambda$ on the basis of equation (2) *via* $\mathcal{P}_\beta$.

Analytical expressions for $\mathcal{P}_\beta = 2R\mathcal{P}_s$ are given in Table 2 for five different rate-based growth models, each based on a rate equation for one of A, V, or r, with growth occurring at constant curvature (please see the Appendix for details of the derivation). Two forms for the rates of change are investigated: (1) constant rate of change, leading to linear time dependence of the observable; and (2) a rate proportional to the characteristic itself, leading to exponential time dependence. Any of these linear or exponential approaches could be plausible under certain conditions; however, we omit a model with linearly decreasing neck radius r, as is justified below. In general, the angle-averaged $\mathcal{P}_\Lambda$ does not have a simple analytical form and must be evaluated numerically by using equation (2). An exception is linear growth in s or A ($ds/dt = 2R/T_2$ for both) leading from $\mathcal{P}_s = (2R)^{-1}$ to $\mathcal{P}_\beta = 2R\mathcal{P}_s = 1$ as discussed as an example following equation (1); as a result

$$\mathcal{P}_\Lambda = \pi/2 - \arcsin(\Lambda - 1), \quad \text{[case I]} \qquad (3)$$

according to equation (2). In the next subsection, the expressions for $\mathcal{P}_\beta$ from Table 2 will be integrated to obtain $\mathcal{P}_\Lambda$ and then compared with measured distributions.

TABLE 2. Calculated probability density $\mathcal{P}_\beta$ for five models of dyad growth. To compare these functions with data from randomly oriented cells, $\mathcal{P}_\beta$ must be averaged using equation (2).

Case	Rate equation	$\mathcal{P}_\beta$
Linear		
I	$ds/dt = 2R/T_2$ or $dA/dt = 4\pi R^2/T_2$	1
II	$dV/dt = (4\pi R^3/3)/T_2$	$3(1 - \beta^2)/2$
III	$dr/dt = -R/T_2$	$\beta/(1 - \beta^2)^{1/2}$
Exponential		
IV	$ds/dt = s \ln 2/T_2$ or $dA/dt = A \ln 2/T_2$	$1/[(\beta + 1)\ln 2]$
V	$dV/dt = V \ln 2/T_2$	$[3(1 - \beta^2)/\ln 2] \div [2 + \beta(3 - \beta^2)]$

These models can be extended without difficulty from dyads to spherocylinders, an idealized shape that contains a cylindrical section of initial length s_0, capped at each end by hemispheres of radius R. We assume that the cylinder first extends from s_0 to $2s_0$, after which the neck constricts while s rises to $2s_0 + 2R$ at the division point. As the fixed parameter of this shape s_0/R becomes large, the time dependence of s, A, and V become ever more similar, such that the behavior of $\mathcal{P}_\beta$ depends mainly on the form of the growth rate (i.e., linear or exponential), not the choice of s, A, or V for its basis. Thus, we narrow our discussion to volume-based growth, which is also a good approximation to length- or area-

based growth. For linear volume growth, one can easily establish that for spherocylinders:

$$\mathcal{P}_\beta = \frac{1}{(2/3 + \beta_0)} \qquad \beta_0 \le \beta \le 2\beta_0 \tag{4a}$$

$$\mathcal{P}_\beta = \frac{(1 - \Delta\beta^2)}{(2/3 + \beta_0)} \qquad 2\beta_0 \le \beta \le 2\beta_0 + 1, \tag{4b}$$

where $\beta_0 = s_0/2R$ and $\Delta\beta = \beta - 2\beta_0$. For exponential volume growth, one obtains

$$\mathcal{P}_\beta = \frac{1}{[(\ln 2)\cdot(2/3 + \beta)]} \qquad \beta_0 \le \beta \le 2\beta_0 \tag{5a}$$

$$\mathcal{P}_\beta = \frac{(1 - \Delta\beta^2)}{2 \ln 2 \cdot \{[1 + \Delta\beta(3 - \Delta\beta^2)/2]/3 + \beta_0\}} \qquad 2\beta_0 \le \beta \le 2\beta_0 + 1. \tag{5b}$$

Both $\mathcal{P}_\beta$ and its first derivative are continuous at $\beta = 2\beta_0$.

Comparisons with Data.—The dimensionless probability density $\mathcal{P}_\Lambda$ is now used for comparing our measurements against the predictions of Table 2 and equations (4) and (5), after averaging over observation angle with equation (2). Because of their better ability to discriminate among cell growth models, we begin with dyadic cells, as shown in Figure 4. The scatter in the data roughly approximates the statistical uncertainties in the individual data points. The most notable feature of Figure 4 is the strong peak in $\mathcal{P}_\Lambda$ at small Λ, exceeding $\mathcal{P}_\Lambda = 2.5$. A successful model must slightly overpredict the maximum value of the peak in order to accommodate its reduction once the smearing effects of experimental uncertainties are taken into account. As $\mathcal{P}_\Lambda$ is normalized to unity, if a model underpredicts the data in one range of Λ, it must overpredict the data elsewhere. The discussion proceeds case by case: the first three cases represent growth that is linear in time, whereas the remaining two cases are exponential.

Case I: linear growth in area or separation. Linear time dependence in s or A yields the same $\mathcal{P}_\Lambda$. Although it slowly decreases with Λ, the predicted $\mathcal{P}_\Lambda$ is much flatter than the data; for example, the $\Lambda = 1$ value of equation (3), namely $\mathcal{P}_\Lambda(1) = \pi/2$ is well below the data of Figure 4 at small Λ, and necessarily above it as $\Lambda \to 2$. The data do not support the model.

Case II: linear growth in volume. At $\Lambda = 1$, this model predicts that $\mathcal{P}_\Lambda$ approaches $3\pi/4 = 2.36$, which is barely sufficient for small Λ; as in cases I and IV, $\mathcal{P}_\Lambda$ then exceeds the data as $\Lambda \to 2$.

Case III: linear shrinkage of septum radius. Here, the expression for $\mathcal{P}_\beta$ in Table 2 is peaked at $\beta = 1$ (or $s = 2R$), the termination of the cell cycle. Even when angle-averaged, it predicts that $\mathcal{P}_\Lambda$ *increases* with Λ, certainly in disagreement with all taxa on Figure 4. Exponential decrease in radius is also in qualitative disagreement with the data, but is not reported in Table 2.

Case IV: exponential growth in area. As shown on Figure 4, this model does not possess the strong peak observed in $\mathcal{P}_\Lambda$ and is somewhat higher than the data as $\Lambda \to 2$. As with cases I and III, the data do not support this model.

Case V: exponential growth in volume. Only this model possesses both the quantitative and qualitative features of $\mathcal{P}_\Lambda$, as seen in Figure 4. It predicts $\mathcal{P}_\Lambda(1) = 3.34$; incorporating experimental uncertainties will reduce the predicted peak and shift its location above $\Lambda = 1$.

Summarizing the results so far for dyads, the data of Figure 4 agree with case V, do not rule out case II, but do not support cases I, III, and IV.

What physical growth mechanisms underlie the equations in Table 2? Linear models assume that change occurs at the same rate throughout the cell cycle no matter what the contents of the cell. Examples of linear models can be found in eukaryotic cells, where the contractile ring may shrink at a constant rate (Biron et al. 2005) and the cell mass grows linearly with time (Killander and Zetterberg 1965). Here, we find that the only linear model not immediately ruled out by data is case II, linear rise in volume, for which agreement with data is marginal at best. Exponential growth may arise from several different mechanistic origins. Case IV corresponds to new surface being created at a rate proportional to the area available to absorb new material—a

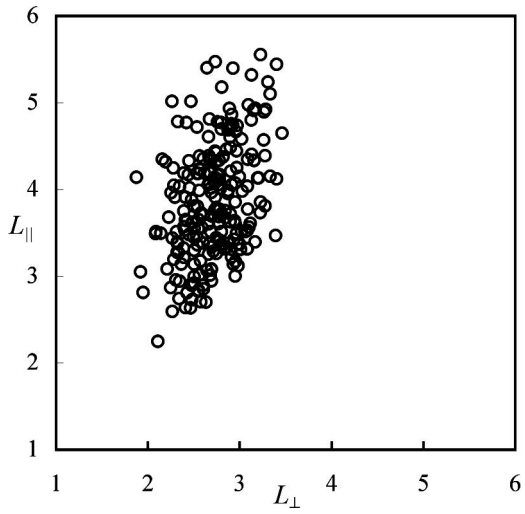

FIGURE 6. Scatter plot of ($L_\perp$, $L_\parallel$) for 224 cells in the *E. moorei* colony reported in Table 1. Dimensions are quoted in microns.

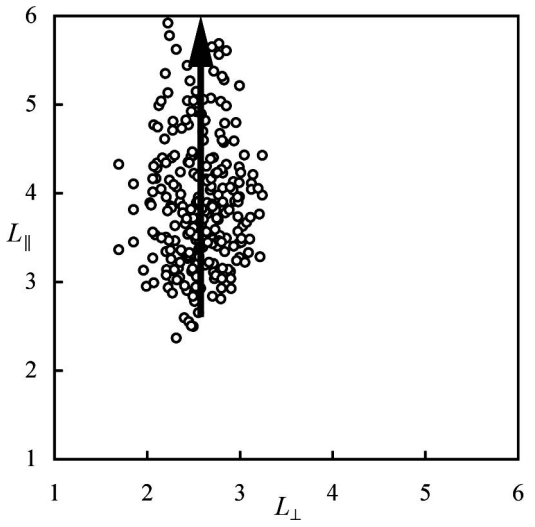

FIGURE 7. Monte Carlo simulation of a rodlike cell colony with exponential volume growth parametrized by $R = 1.3$ μm, $s_0 = 0.5$ μm, and experimental uncertainty $\sigma = 0.3$ μm. The vertical arrow is the idealized growth trajectory. Dimensions are quoted in microns.

logical possibility but not supported by Figure 4. Lastly, case V arises if new volume is created at a rate proportional to the cell's contents, which is the only scenario to describe the data comfortably.

Cylindrical cells cannot select among growth models to the same extent as can dyads, but they are a distinct morphology and could in principle obey a different mechanism for growth. Here, quantities such as $\mathcal{P}_\Lambda$ can distinguish between linear and exponential growth only for high statistics data, being generally insensitive to whether growth is driven by *s*, *A*, or *V*. The angle-averaged prediction for $\mathcal{P}_\Lambda$ is displayed in Figure 5 for linear and exponential growth in volume for $\beta_0 = 0.2$. Compared with the $\beta_0 = 0$ (dyad) curve in Figure 4, the peak in $\mathcal{P}_\Lambda$ at $\Lambda \sim 1$ is suppressed for spherocylinders in Figure 5, and the probability density is spread to regions both below the peak, and above $\Lambda = 2$. Accounting for experimental uncertainties will smear the peak further. Although the agreement with the data displayed for *E. moorei* is not perfect for $\beta_0 = 0.2$, nevertheless the predictions are consistent. The quality of the agreement is degraded if β_0 is raised to 0.5. Exponential elongation has been established with good statistics for a variety of modern bacilli: *B. subtilis* (Sharpe et al. 1998), *B. cereus* (Collins and Richmond 1962), and *E. coli* (Koppes and Nanninga 1980), indicating that the exponential growth mode may have characterized rodlike bacteria for several billion years.

Correlations of ($L_\perp$, $L_\parallel$).—To probe further into the cell cycle we examine the correlations in $L_\perp$ and $L_\parallel$, which are removed when the dimensionless variable $\Lambda = L_\parallel/L_\perp$ is taken. A scatter plot of ($L_\perp$, $L_\parallel$) from the bacillus-like *E. moorei* colony of Table 1 is displayed in Figure 6, where the coordinate origin has been shifted to visually exaggerate the distribution. The vertical trend is what one would expect from a model of elongation of a cylinder at constant width: for cells lying perpendicular to the viewing axis ($\theta = \pi/2$), one would expect ($L_\perp$, $L_\parallel$) to run from ($2R$, $2R + s_0$) to ($2R$, $4R + 2s_0$). To compare these data quantitatively with a model, one would have to incorporate both the random distribution in θ, which will shift the distribution toward the $L_\parallel = L_\perp$ line, and experimental uncertainties, which tend to broaden the distribution horizontally (although the behavior is more complex near $L_\perp = L_\parallel$ because of the definitions of $L_\perp$ and $L_\parallel$). A Monte Carlo simulation of the cell cycle including these effects is shown in Figure 7; this is a model with exponential volume growth and $R = 1.3$ μm, $s_0 = 0.5$ μm ($\beta_0 = 0.2$), and experimental uncertainty in ($L_\perp$, $L_\parallel$) governed

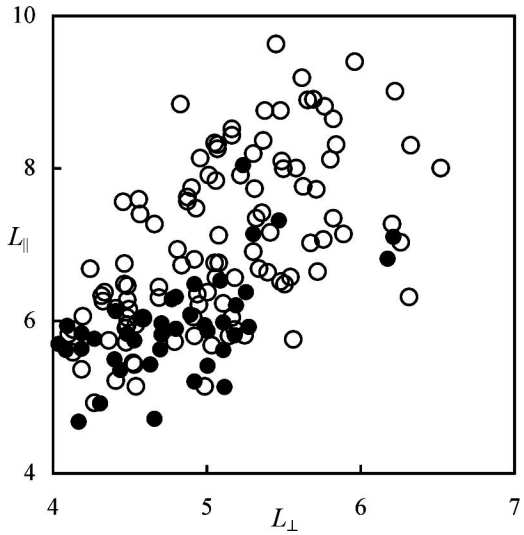

FIGURE 8. Scatter plot of ($L_\perp$, $L_\parallel$) for 156 cells in the *E. belcherensis capsulata* colony reported in Table 1. Visible dyads (doublets) are indicated by open circles, and singlets are displayed as solid disks. Dimensions are quoted in microns. For clarity of presentation, the scale of the x-axis is double that of the y-axis.

by a normal distribution with $\sigma = 0.3$ μm. The vertical arrow indicates the trajectory in the idealized $\sigma = 0$ limit. The simulation is seen to be in qualitative agreement with the data. Unfortunately, the interpretation of σ is clouded because it represents not just experimental uncertainty but also effects arising from distributions in daughter size or division time (Koch and Schaechter 1962; Rosenberger et al. 1978; Sharpe et al. 1998; see also Koch 1983).

Compared with rodlike *E. moorei*, potentially more information can be extracted from scatter plots of ($L_\perp$, $L_\parallel$) for dyads, where the added feature is classification of the cell according to the presence of a visible neck or junction ring. We will refer to cell pairs *with* a visible ring as doublets and *without* as singlets, recognizing that physical dyads may appear as singlets when the orientation angle $\theta \sim 0$. A scatter plot of the *E. belcherensis capsulata* data is displayed in Figure 8; note that the x and y scales are inequivalent. The singlets tend to be distributed along the $x = y$ line, corresponding to uniform expansion of the cell early in its cycle. The doublets are distributed more vertically, corresponding to the formation of the symmetry axis and division plane. For such a two-step picture, the idealized trajectory for dyads would be a straight line along $x = y$ starting at ($2R$, $2R$) followed by a straight, non-vertical line to ($2R$, $4R$). Although the data aren't strong enough to support this picture quantitatively, they are nevertheless suggestive. Each dyad colony of Table 1 has a different fraction of visible dyads, and the scatter plots of each colony suggest that the larger this fraction, the less time is spent in the initial phase of uniform expansion. Given the ambiguity of identifying visible dyads when θ is near zero, we cannot yet quantitatively assign a time fraction for the expansion phase. It's worth mentioning that populations of modern diplococcal cyanobacteria display the same qualitative features as Figure 8 (C. Forde and D. H. Boal unpublished data): the fraction and distribution of visible dyads, and the distribution of singlets along the $L_\parallel = L_\perp$ line are similar in both the ancient and modern cells.

Conclusions

Adopting a digital algorithm for characterizing cell shapes from good-resolution CCD images, we have measured size and shape distributions of two-billion-year-old dyads and bacillus-like cells. To interpret these distributions, five different rate-based models were developed for dyad growth, and two for bacillus growth; the models easily accommodate numerical averaging over the cell's orientation angle with respect to the observer. In this paper, more emphasis has been placed on dyads than on rodlike bacilli, because the geometry of the former is more suitable for distinguishing among growth models. For four types of microfossils, the shape distributions are consistent with exponential volume growth at constant surface curvature, obeying a rate dV/dt proportional to cell volume V: the greater the cell's contents, the faster it grows. The data do not rule out linear volume growth, but they are inconsistent with linear or exponential growth in area (or separation s) or with linear decrease in the radius of the septum. Scatter plots of ($L_\perp$, $L_\parallel$) demonstrate that dyad growth may include a short initial phase of uniform expansion before the axis of elongation appears. We continue to investigate whether the extra information contained in scatter plots

may prove useful in establishing the identity of microfossils through comparison with modern cyanobacteria.

Qualitatively, the most important term driving the shape of these ancient cells is the increase in the cell's contents, which the surface area accommodates but does not direct. The behavior is consistent with exponential elongation observed in modern cylindrical *B. subtilis* (Sharpe et al. 1998), *B. cereus* (Collins and Richmond 1962) and *E. coli* (Koppes and Nanninga 1980). Linear volume growth as seen in modern eukaryotes is not dismissed by the microfossil data, but is certainly less likely. Thus, the growth modes of these two morphologically distinct groups of 2-Ga microfossils (dyads and bacillus-like cells) are closer to modern prokaryotes than modern eukaryotes, in spite of the presence of dark interiors in some taxa that might be suggestive of nuclei.

We have attempted to identify the presence of a wall at the interface between cell compartments by measuring the optical intensity profile along the symmetry axis of the dyad. Referring to the orientation of the dyad in Figure 2 (top view), light traveling through only one of the subunits in the dyad passes through two wall regions, whereas light traveling through the center passes through three. If the central wall has the same thickness as the external cell wall, then an absorption intensity profile taken along the symmetry axis of the dyad should display three minima in roughly a 2:3:2 ratio, ignoring the angle-dependent path length of light through the walls. We have succeeded in analyzing only a handful of *E. belcherensis capsulata* and found that the intensity minimum of the overlap region is 0–70% larger than that of the individual subunits. While suggestive, this range is too large to allow a conclusion to be drawn about the presence of an internal wall; a technique with finer resolution than optical microscopy will most likely be needed to resolve this question. Further, the use of three-dimensional image reconstruction would permit the cell shapes to be determined directly, eliminating the angle-averaging procedure of the approach taken here (for example, Grotzinger et al. 2000; Xiao 2002).

Acknowledgments

The authors wish to thank H. Hofmann for extensive conversations regarding Belcher Island microfossils. We are also indebted to J. Dougherty, curator of the microfossil collection at the Geological Survey of Canada in Ottawa, both for facilitating access to the collection and for many patient discussions. We thank A. Knoll for his comments on the initial version of this manuscript. This work is supported in part by the Natural Sciences and Engineering Research Council of Canada.

Literature Cited

Barghoorn, E. S., and S. A. Tyler. 1965. Microorganisms from the Gunflint chert. Science 147:563–577.

Biron, D., E. Alvarez-Lacalle, T. Tlusty, and E. Moses. 2005. A molecular model of the contractile ring. Physical Review Letters 95:098102.

Boal, D. H. 2002. Mechanics of the cell. Cambridge University Press, Cambridge.

Bramhill, D. 1997. Bacterial cell division. Annual Reviews of Cell and Developmental Biology 13:395–424.

Collins, J. F., and M. H. Richmond. 1962. Rate of growth of *Bacillus cereus* between divisions. Journal of General Microbiology 28:15–33.

Fryer, B. 1972. Age determinations in the Circum-Ungava geosyncline and the evolution of Precambrian iron-formations. Canadian Journal of Earth Sciences 9:652–663.

Furnes, H., N. R. Banerjee, K. Muehlenbachs, H. Staudigel, and M. de Wit. 2004. Early life recorded in Archean pillow lavas. Science 304:578–581.

Golubic, S., and H. J. Hofmann. 1976. Comparison of modern and mid-Precambrian Entophysalidaceae (Cyanophyta) in stromatolitic algal mats: cell division and degradation. Journal of Paleontology 50:1074–1082.

Grotzinger, J. P., W. A. Watters, and A. H. Knoll. 2000. Calcified metazoans in thrombolite-stromatolite reefs of the terminal Proterozoic Nama Group, Namibia. Paleobiology 26:334–359.

Hall, M. N., M. Raff, and G. Thomas, eds. 2004. Cell growth: control of cell size. Cold Spring Harbor Laboratory Press, Cold Spring Harbor, N.Y.

Hofmann, H. J. 1975. Stratiform Precambrian stromatolites, Belcher Islands, Canada: relations between silicified microfossils and microstructure. American Journal of Science 275:1121–1132.

———. 1976. Precambrian microflora, Belcher Islands, Canada: significance and systematics. Journal of Paleontology 50: 1040–1073.

Killander, D., and A. Zetterberg. 1965. A quantitative cytochemical investigation of the relationship between cell mass and initiation of DNA synthesis in mouse fibroblasts in vitro. Experimental Cell Research 40:12–20.

Knoll, A. H., and E. S. Barghoorn. 1976. A Gunflint-type microbiota from the Duck Creek Dolomite, Western Australia. Origins of Life 7:417–423.

———. 1977. Archean microfossils showing cell division from the Swaziland System of South Africa. Science 198:396–398.

Koch, A. L. 1983. The surface stress theory of microbial morphogenesis. Advances in Microbial Physiology 24:301–366.

Koch, A. L., and M. Schaechter. 1962. A model for statistics of the cell division process. Journal of General Microbiology 29: 435–454.

Koppes, L. J. H., and N. Nanninga. 1980. Positive correlation between size at initiation of chromosome replication in *Escherichia coli* and size at initiation of cell constriction. Journal of Bacteriology 143:89–99.

Mojzsis, S. J., G. Arrhenius, K. D. McKeegan, T. M. Harrison, A. P. Nutman, and C. R. L. Friend. 1996. Evidence for life on Earth before 3,800 million years ago. Nature 384:55–59.

Moore, E. S. 1918. The iron formation on Belcher Islands, Hudson Bay, with special reference to its origin and its associated algal limestones. Journal of Geology 26:412–438.

Murray, A., and T. Hunt. 1993. The cell cycle: an introduction. Oxford University Press, Oxford.

Rasmussen, B. 2000. Filamentous microfossils in a 3,235-million-year-old volcanogenic massive sulphide deposit. Nature 405:676–679.

Rosenberger, R. F., N. B. Grover, A. Zaritsky, and C. L. Woldringh. 1978. Surface growth in rod-shaped bacteria. Journal of Theoretical Biology 73:711–721.

Rosing, M. T. 1999. ^{13}C-depleted carbon microparticles in >3700 Ma sea-floor sedimentary rocks from West Greenland. Science 283:674–676.

Schidlowski, M. 1988. A 3,800-million-year isotopic record of life from carbon in sedimentary rocks. Nature 333:313–318.

Schopf, J. W. 1993. Microfossils of the Early Archean Apex chert: new evidence of the antiquity of life. Science 260:640–646.

Schopf, J. W., and B. M. Packer. 1987. Early Archean (3.3-billion to 3.5 billion-year-old) microfossils from Warrawoona Group, Australia. Science 237:70–73.

Sharpe, M. E., P. M. Hauser, R. G. Sharpe, and J. Errington. 1998. *Bacillus subtilis* cell cycle as studied by fluorescence microscopy: constancy of cell length at initiation of DNA replication and evidence for active nucleoid partitioning. Journal of Bacteriology 180:547–555.

Shen, Y., D. Canfield, and R. Buick. 2001. Isotopic evidence for microbial sulphate reduction in the early Archean ocean. Nature 410:77–81.

Smith, R. E. 1968. Grain size measurement in thin section and in grain mount: reply to comment by Sahu. Journal of Sedimentary Research 38:268–271.

Timofeev, B. V. 1979. Mikrofitossilii Pechenskoi serii. Pp. 119–120 *in* B. V. Sokolov, ed. Paleontologiya dokembriya i rannega Kembriya. Nauka, Leningrad.

van Zuilen, M. A., A. Lepland, and G. Arrhenius. 2002. Reassessing the evidence for the earliest traces of life. Nature 418: 627–630.

Walsh, M. M., and D. R. Lowe. 1985. Filamentous microfossils from the 3,500-Myr-old Onverwacht Group, Barberton Mountain Land, South Africa. Nature 314:530–532.

Xaio, S. 2002. Mitotic topologies and mechanics of Neoproterozoic algae and animal embryos. Paleobiology 28:244–250.

Appendix

The purpose of this appendix is to provide a sketch of the mathematical steps leading to the analytical distributions in Table 2. The starting point for the calculations is an expression for the surface area or volume of the idealized geometries chosen to represent the shapes of dyads or bacillus-like cells. Because it is analytically simpler, dyad geometry is discussed first.

Given the narrow distribution observed for the diameter of dyads, their assumed geometry will be that of two spherical caps of fixed radius R intersecting at a ring (or neck) of varying radius r, as in Figure 2. The separation between the centers of the caps is s, which can range from $s = 0$ at the beginning of the cell cycle to $s = 2R$ at the division point. It is not difficult to show that the total surface area A and total enclosed volume V of the dyad are as follows:

$$A = 4\pi R^2(1 + s/2R) = 4\pi R^2(1 + \beta) \quad \text{(dyad)} \quad \text{(A1)}$$

$$V = (4\pi R^3/3)\{1 + (s/2R)\cdot[3 - (s/2R)^2]/2\}$$
$$= (4\pi R^3/3)[1 + \beta\cdot(3 - \beta^2)/2]. \quad \text{(dyad)} \quad \text{(A2)}$$

In the limit $s = 0$, these expressions have their single-sphere values, and at $s = 2R$ the area and volume are doubled. The combination $s/2R$ appears so frequently in what follows that it is easier to work with the second representation in equations (A1) and (A2), where the dimensionless quantity

$$\beta = s/2R \quad \text{(A3)}$$

has been introduced. The volume of rodlike cells will be presented below.

From the viewpoint of measurement accuracy and interpretation, the geometrical attribute of greatest interest is the projection of the separation s onto the observation plane of a microscope. Thus, the measurement process yields information on $\mathcal{P}_s$, a probability density (per unit s). The simple example $\mathcal{P}_s = (2R)^{-1}$ for linear growth in s is given in the text; here we describe the more relevant situation of exponential volume growth

$$V(t) = V_0 \exp(\ln 2\ t/T_2). \quad \text{(A4)}$$

In this equation, the volume doubles from its initial value V_0 in a time T_2. To obtain $\mathcal{P}_s$ we assume steady-state conditions such that $\mathcal{P}_s = [T_2\cdot(ds/dt)]^{-1}$. As will become obvious momentarily, it is less cumbersome to work with $\mathcal{P}_\beta$ than with $\mathcal{P}_s$, for which

$$\mathcal{P}_\beta = [T_2\cdot(d\beta/dt)]^{-1}. \quad \text{(A5)}$$

The two probability densities are related by $\mathcal{P}_\beta = (ds/d\beta)\mathcal{P}_s = 2R\mathcal{P}_s$, according to equation (A3).

Armed with the time-dependence of the volume in equation (A4), one can invert either representation of equation (A2) to obtain the functions $s(t)$ or $\beta(t)$. However, equation (A2) is cubic in s or β, so the inversion is cumbersome; in fact, it's unnecessary, as all that is needed to solve equation (A5) is the time derivative $d\beta/dt$. Rearranging equation (A4) to read

$$t = (T_2/\ln 2)\ln(V/V_0), \quad \text{(A6)}$$

and replacing $V(t)$ by equation (A2), one obtains

$$dt/d\beta = (T_2/\ln 2)\cdot 3(1 - \beta^2)/[2 + \beta\cdot(3 - \beta^2)]. \quad \text{(A7)}$$

Equation (A7) then may be substituted into equation (A5) to obtain

$$\mathcal{P}_\beta = [3(1 - \beta^2)/\ln 2]/[2 + \beta\cdot(3 - \beta^2)], \quad \text{(A8)}$$

which is the result quoted in Table 2 for exponential volume growth of dyads.

The idealized shape we choose for representing bacillus-like cells is the spherocylinder: a uniform cylinder of radius R capped at each end by hemispheres of the same radius. If the minimum cylinder length at the start of the cell cycle is s_0 (where s is still the distance between the centers of curvature of the endcaps), then s runs from s_0 to $2s_0 + 2R$ by the time the cell has doubled at $t = T_2$. Alternatively, β runs from β_0 ($= s_0/2R$) to $2\beta_0$ as the length of the cylindrical section doubles, and then to $2\beta_0 + 1$ as two new hemispheres are formed at the division plane of the cylinder. Expressed in terms of β, the volume of the spherocylinder is

$$V = (4\pi R^3/3)\cdot(1 + 3\beta/2)$$
$$\beta_0 \le \beta \le 2\beta_0 \quad \text{(A9a)}$$

$$V = (4\pi R^3/3)\cdot[1 + \Delta\beta(3 - \Delta\beta^2)/2)] + 4\pi R^3\beta_0$$
$$2\beta_0 \le \beta \le 2\beta_0 + 1 \quad \text{(A9b)}$$

where

$$\Delta\beta = \beta - 2\beta_0. \quad \text{(A10)}$$

These expressions can be manipulated as above to yield $\mathcal{P}_\beta$, although the mathematics is slightly more cumbersome because of the change in functional form at $2\beta_0$. Again, it is not necessary to solve for $\beta(t)$ or $s(t)$, simply finding their time derivative is sufficient. However, here it is more convenient to use $(d\beta/dt) = (d\beta/dV)\cdot(dV/dt)$ to derive equation (5) for exponential volume growth.

In the lab, it may be possible to manipulate cells such that their symmetry axes lie in observational plane, even if they are not parallel to each other. In such circumstances, $\mathcal{P}_\beta$ or $\mathcal{P}_s$ can be measured directly. However, the microfossil cell colonies that are studied here have random orientations in three dimensions, which forces us to average over the angle θ in Figure 2 (the angle between the symmetry axis and the viewing axis) when predicting the distribution of shapes as projected onto the observational plane. Now, the projected length and width of the idealized shapes here are $L_\parallel = 2R + s\cdot\sin\theta$ and $L_\perp = 2R$, respectively, such that the dimensionless ratio $\Lambda = L_\parallel/L_\perp$ is given by

$$\Lambda = 1 + (s/2R)\sin\theta = 1 + \beta\sin\theta. \tag{A11}$$

The probability density $\mathcal{P}_\Lambda$ of Λ is then obtained from $\mathcal{P}_s$ or $\mathcal{P}_\beta$ by averaging over θ, as in

$$\mathcal{P}_\Lambda\, d\Lambda = \int \mathcal{P}_\beta\, d\beta\sin\theta\, d\theta. \tag{A12}$$

Using equation (A11) to obtain $(d\Lambda/d\theta) = \beta\cos\theta$ as well as expressions for $\sin\theta$ and $\cos\theta$, we can rewrite equation (A12) as

$$\mathcal{P}_\Lambda = \int \mathcal{P}_\beta \frac{[(\Lambda - 1)/\beta]}{[\beta^2 - (\Lambda - 1)^2]^{1/2}}\, d\beta, \tag{A13}$$

which is equation (2). Note that the integration limits depend on the value of Λ chosen for $\mathcal{P}_\Lambda$: the lower limit is the larger of $\Lambda - 1$ or β_0 and the upper limit is $1 + 2\beta_0$.